Research Article Wiley Online Library ELECTROANALYSIS

doi.org/10.1002/elan.202100701

In Situ Growth of $Ni(OH)_2$ Nanoparticles on 316L Stainless Steel Foam: An Efficient Three-dimensional Non-enzymatic Glucose Electrochemical Sensor in Real Human Blood Serum Samples

Widad Drissi,[a] Mohamed Lyamine Chelaghmia,*[a] Mouna Nacef,[a] Abed Mohamed Affoune,[a] Hamid Satha,[b] Rafiaa Kihal,[a] Hassina Fisli,[c] Chahira Boukharouba,[a] and Maxime Pontié[d]

Abstract: For the first time, nickel hydroxide nanoparticles ($Ni(OH)_2$ NPs) grown on 316L stainless steel foam were used as a non-enzymatic electrochemical glucose sensor. The $Ni(OH)_2$/SSF-316L was elaborated by applying a simple ultrafast CV method without nickel salts addition. $Ni(OH)_2$/SSF-316L was characterized by SEM and XRD. The electrochemical behavior was investigated by CV, EIS, and amperometric measurements. The fabricated sensor revealed higher sensitivity 1062 μA $mM^{-1}cm^{-2}$, wide linear range from 1.0 μM to 4.0 mM with a low detection limit of 2.0 μM and good selectivity. In addition, real sample analysis was performed for controlled glucose in real blood serum.

Keywords: Nickel hydroxide · 316L stainless steel foam · Glucose non-enzymatic sensor · Electrochemical impedance spectroscopy

1 Introduction

Diabetes mellitus disease has become a major public health problem in recent decades, representing around 5 % of the world's population [1–3]. Therefore, rapid and sensitive blood glucose detection has gained enormous importance for diagnosing and managing diabetic patients [4–6]. Several methods have been applied for quantitative glucose detection [7–12]. Electrochemical sensors exhibit superior performance towards glucose detection than traditional methods, owing to their simplicity, low cost, and reliability [13–16].

Then, electrochemical glucose sensors can be divided into enzyme-based and non-enzymatic sensors based on their detection mechanisms.

Typically, electrochemical enzymatic sensors with the glucose oxidase enzyme (GOD) show good selectivity and high sensitivity. However, they still suffer from a complex manufacturing procedure, limited temperature, unfavorable micro-environment factors, and the non-negligible response of some interfering species [17–21].

Therefore, non-enzymatic sensors, based on a wide range of metals, alloys, metal oxides, and metal hydroxides [22–35], are considered a potential substitute for enzymatic sensors through their high sensitivity and stability enzyme-free from activity [23,24]. Among these non-enzymatic sensors, nickel-based sensors exhibit excellent electrocatalytic activity for glucose oxidation. They have attracted many researchers due to their low toxicity and high stability [25–35]. Their electrocatalytic performance depends especially on the formation of $Ni(OH)_2$ as a strong oxidant of organic compounds in alkaline solutions [36–42].

Recently, significant progress in fabricating metallic or intermetallic foam-like materials has been made [43–48]. These new low-density materials offer a very interesting combination of physical and chemical properties, giving them a wide application field [45–47]. Among the different metallic foams, nickel foam (NF) is an ideal scaffold to grow $Ni(OH)_2$ due to its many advantages, such as high conductivity, three-dimensional network structure, high specific surface area, and strong mass transfer ability [48–51]. In addition, Ni foam has excellent properties, such as low-density and low-cost. It has been used as a substrate for glucose sensors [50].

Many porous metal foams could be used as substrates for the deposition of $Ni(OH)_2$, such as 316L stainless steel

[a] W. Drissi, M. Lyamine Chelaghmia, M. Nacef, A. Mohamed Affoune, R. Kihal, C. Boukharouba
Laboratoire d'Analyses Industrielles et Génie des Matériaux, Université 8 Mai 1945 Guelma 24000, BP 401, Guelma, Algeria
E-mail: chelaghmia.mohamedlyamine@univ-guelma.dz
amine_chelaghmia@yahoo.fr
[b] H. Satha
Laboratoire LSPN, Université 8 Mai 1945 Guelma 24000, BP 401, Guelma, Algeria
[c] H. Fisli
Laboratoire de Chimie Appliquée, Université 8 Mai 1945 Guelma 24000, BP 401, Guelma, Algeria
[d] M. Pontié
Groupe Analyses et Procédés (GA&P), Angers univ, Faculty of Sciences, 2 Bd. Lavoisier 49045 Angers Cedex 1 France

Supporting information for this article is available on the WWW under https://doi.org/10.1002/elan.202100701

foam (SSF-316L) and Inconel foam (IncF). Compared to other metals foam, these two foams exhibit better stability, particularly excellent resistance to corrosion and oxidation [52,53]. However, to date, there are no reports in the literature on the use of 316L stainless steel foam for non-enzymatic glucose detection.

To our knowledge, this is the first report on modifying an inactive commercially three-dimensional 316L stainless steel foam electrode into a highly sensitive non-enzymatic glucose electrode through the direct in situ growth of nickel hydroxides nanoparticles without adding nickel salts via a simple one-step electrochemical method. The electrochemical impedance spectroscopy (EIS), cyclic voltammetry (CV), and amperometric techniques were used to evaluate the electroanalytical performance of the $Ni(OH)_2$/SSF-316L sensor. This non-enzymatic sensor is also suitable for detecting glucose in human blood serum with excellent stability and good reproducibility.

2 Experimental Details

2.1 Chemicals and Reagents

The macroporous 316L stainless steel foam (thickness: 1.5 mm, pore density: 110 PPI) was purchased from Atlantum Company (Munich, Germany). Table 1 lists its chemical composition. D-(+)-glucose (Glc), Sucrose (Suc), sodium hydroxide (NaOH), L-ascorbic acid (AA), uric acid (UA), and acetaminophen (AP) were bought from Sigma-Aldrich. Three fresh human blood serum samples were taken from diabetic and healthy people who volunteered. All experiments were carried out in compliance with the local hospital's ethical guidelines. The samples were first centrifuged at 10,000 rpm for 30 min to precipitate any proteins, after that, the top phase was filtered for coming tests. The reagents are all analytical grade and are used directly as received.

2.2 Preparation of $Ni(OH)_2$/SSF-316L

The commercial 316L stainless steel foam substrate (0.5 × 0.5 cm) was soaked and sonicated consecutively in acetone, DI water, and absolute ethanol for 15 min. Then, it was dried at 105 °C for 2 h. The $Ni(OH)_2$ NPs were grown on SSF-316L substrate using multiple scan cyclic voltammetry until reproducible curves of active and stable $Ni(OH)_2$ NPs were obtained. The consecutive cyclic voltammograms ranged from 0.1 to 0.65 V in 0.1 M NaOH acquired at a fixed scan rate of 50 $mV\,s^{-1}$ for 100 cycles.

Table 1. Chemical composition of SSF-316L foam (wt.%).

S	P	C	Si	Mn	Mo	Ni	Cr	Fe
0.001	0.017	0.025	0.56	1.21	2.16	11.1	17.6	Bal

2.3 Instruments

All electrochemical experiments were performed with a potentiostat (Princeton Applied Research, AMETEK, USA) at room temperature. The typical three-electrode system configuration was used. The reference electrode was Ag/AgCl (Sat. KCl), the counter electrode was a Pt wire, and the working electrode was unmodified SSF-316L or modified $Ni(OH)_2$/SSF-316L.

The electrocatalytic performances of the electrodes were carried out by CV, EIS, and amperometric measurements.

CV measurements were taken at a fixed scan rate of 50 $mV\,s^{-1}$ in the potential range of 0 to 0.65 V. Amperometric measurements were performed at an applied potential of 0.55 V in stirring 0.1 M NaOH. EIS technique was utilized in the frequency range of 100 kHz to 0.1 Hz, with an amplitude voltage of 10 mV. 10 µL of the serum blood sample was added to 10 mL of 0.1 M NaOH solution to detect a real sample. The current response was recorded at an applied potential of +0.55 V.

Scanning electron microscopy (SEM) analyses were performed using a JEOL JSM-IT 100. Electrode structure was investigated by X-ray diffraction (XRD) using a D8 Advance Brucker diffractometer (CuKα1, 2).

3 Results and Discussion

3.1 Electrochemical Formation and Characterization of $Ni(OH)_2$/SSF-316L Foam

Figure 1a represents the overlay of the consecutive cyclic voltammograms (CV grams) in the potential range from 0.1 to 0.65 V in 0.1 M NaOH, acquired at 50 $mV\,s^{-1}$ for 100 cycles. A quasi-reversible redox system appears with only one redox couple in all CV curves, which may result in the redox process of Ni^{2+}/Ni^{3+} at about 0.57 and 0.43 V, respectively, with a peak potential separation (ΔE_p) of 140 mV, and indicates that electrochemical activity of SSF-316L electrode originating from following redox mechanism:

$$Ni + 2OH^- \rightarrow Ni(OH)_2 + 2e^- \quad (1)$$

$$Ni(OH)_2 + OH^- \rightarrow NiOOH + H_2O + 1e^- \quad (2)$$

Moreover, increasing the number of cycles made these peaks more intense because more $Ni(OH)_2$ films were formed onto the electrodes' surface. Until the 100th cycle, the anodic and cathodic peak current values become stable (Figure 1b), suggesting that the entire Ni metal on the stainless steel surface was completely converted into $Ni(OH)_2$.

Figure 2(a–d) illustrates the structure and morphology of $Ni(OH)_2$/SSF-316L. Figure 2 shows the low (a) and medium (b) magnitude SEM images of the stainless steel foam. The foam has almost spherical pores with a smooth surface, which are connected by multiple small windows

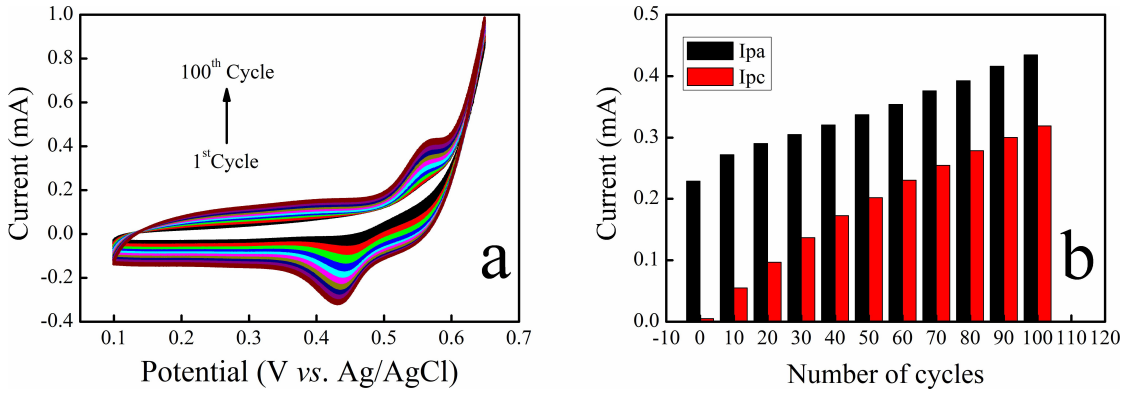

Fig. 1. (a) 100-cycles CV curves recorded on $Ni(OH)_2$/SSF-316L electrode preparation at 50 $mV s^{-1}$, (b) Illustration of anodic and cathodic peak currents *vs.* plot the number of scan cycles.

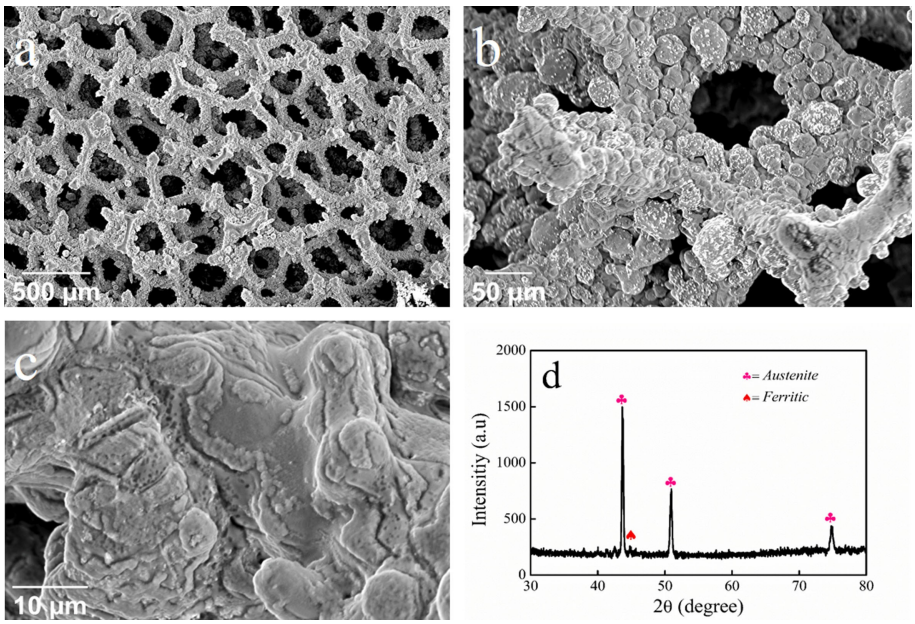

Fig. 2. (a) Low-, (b) medium, and (c) high-magnification SEM images of $Ni(OH)_2$/SSF-316L, (d) XRD patterns of $Ni(OH)_2$/SSF-316L.

creating an open cell structure. At the same time, the foam surface became rougher after only one cycle in alkaline solution with the emergence of many small particles (Figure 2b). Figure 2c shows the high magnitude SEM image of $Ni(OH)_2$/SSF-316L. It can be noted that the foam surface is covered with a thin film of $Ni(OH)_2$ nanoparticles.

This foam's three-dimensional (3D) architecture results in a large surface area on which electrochemical reactions can occur, making the stainless steel foam a very attractive material for various applications. Figure 2d shows the XRD patterns of the as-modified stainless steel foam. The result shows that stainless steel foam is mainly composed of austenite phase and a small amount of ferrite. The strong diffraction peaks corresponding to crystal faces (111), (200), and (220) of face-centered cubic (fcc) austenite (γ phase) were positioned at $2\theta = 43.56$, 50.61 and 74.81°, respectively.

3.2 Electrochemical Properties of the $Ni(OH)_2$/SSF-316L Foam

CV and EIS were carried out in 1.0 mM $[Fe(CN)_6]^{3-/4-}$ and 0.1 M Na_2SO_4 as redox probe solution to evaluate the electrochemical behavior and study the conductivity and charge transfer kinetics of the unmodified and modified electrodes.

Figure 3a displays the CV grams of the unmodified and modified electrodes with a pair of well-defined peaks of $[Fe(CN)_6]^{3-/4-}$ redox species solution. As it can be seen, the difference in potential between the anodic and cathodic peaks (ΔEp) was slightly decreased to 0.541 V at the $Ni(OH)_2$/SSF-316L compared to 0.585 V for unmodi-

fied SSF-316L. Furthermore, the redox peak currents at the $Ni(OH)_2$/SSF-316L electrode are larger than that at the unmodified electrodes.

These results reveal that the growth of Nickel hydroxide NPs on the SSF-316L substrate improved the electron transfer on the electrode interface and increased the electrode surface area. The Nyquist plots illustrate a semicircle part related to the electron transfer limited process, which is equivalent to the electron transfer resistance (R_{ct}) in EIS (Figure 3b).

By fitting the impedance data with the equivalent circuit (Figure 3b, inset), the $Ni(OH)_2$/SSF-316L exhibited remarkably lower values of R_{ct} (179.5 Ohm) than the unmodified electrode (547.3 Ohm). Hence, the EIS results are consistent with the above results from CV and demonstrate that the SSF-316L substrate was successfully modified. The growth of $Ni(OH)_2$ nanoparticles on the porous SSF-316L surface improved the electrochemical properties of the modified electrode.

The electrochemical surface areas of SSF-316L and $Ni(OH)_2$/SSF-316L electrodes were calculated from the slope of anodic peak current $I_p$versus square root of scan rate $v^{1/2}$ curves (Supporting Information, Figure S1) for a known concentration of $[Fe(CN)_6]^{3-/4-}$ based on the Randles-Sevcik's equation [54]:

$$I_p = 0.436\, nFAC\sqrt{\frac{nFDv}{RT}} \tag{3}$$

where, I_p is the peak current (A), C is the bulk concentration of $[Fe(CN)_6]^{3-/4-}$ (mol.cm^{-3}), and D is the diffusion coefficient (cm^2.s^{-1}). From the calculated slopes belonging to each plot extracted as Ipa versus $v^{1/2}$. The electrochemical active surface areas were 0.11 and 0.23 cm^2 for SSF-316L and $Ni(OH)_2$/SSF-316L, respectively.

The electrochemical behavior of the Ni^{2+}/Ni^{3+} redox process on the modified electrode was also studied by cyclic voltammetry in 0.1 M NaOH solution at various scan rates (Figure 4a). When the scan rate increases, the values of the peak's currents are proportional to scan rates in the range of 5–1000 mV s^{-1}, whereas the potentials of the anodic peak (E_{pa}) and cathodic peak (E_{pc}) undergo positive and negative shifts, respectively.

These shifts can be related to rapid electron transfer kinetics over this range of scan rates [55]. Besides that, a linear proportionality between peaks currents and the square root of scan rate was found (Figure 4b), indicating a diffusion-controlled process over the $Ni(OH)_2$/SSF-316L electrode surface. The electrode surface coverage (Γ^*) of the redox species of $Ni(OH)_2$/SSF-316L can be determined using the following equation [56]:

$$I_p = \left(\frac{n^2F^2}{4RT}\right)vA\Gamma^* \tag{4}$$

where, I_p is the peak current in ampere, and A is the electrode surface area in cm^2. According to the average of both anodic and cathodic results, the value of Γ^* was estimated to be 3.51×10^{-8}, which roughly corresponds to 35 monolayers of surface species for Ni.

For the surface-confined electroactive species, the electron transfer coefficient (α_s) and electron transfer rate constant (K_s) can be estimated from the CV grams using Laviron's theory [57]. For peak-to-peak potential separation $\Delta E_p > 200/n$ mV, anodic and cathodic potentials are expressed as follows:

$$E_{pa} = E^o + [RT/(1-\alpha)nF]lnv \tag{5}$$

$$E_{pc} = E^o - (RT/\alpha nF)lnv \tag{6}$$

$$lnK_s = \alpha ln(1\text{-}\alpha) + (1\text{-}\alpha)ln\alpha - \boldsymbol{ln}\left(\frac{RT}{nFv}\right) - \alpha(1-\alpha)nF\Delta E_p/RT \tag{7}$$

where, $E^o$is the standard electrode potential, while the other terms have their usual meanings. The peak potential is linearly dependent on the logarithmic function at higher scan rates [400–1000 mV s^{-1}] (Figure 4c). Using the linear regression and Eqs. (5)-(7), α_s and K_s values were obtained as 0.41 and 0.21 s^{-1}, respectively.

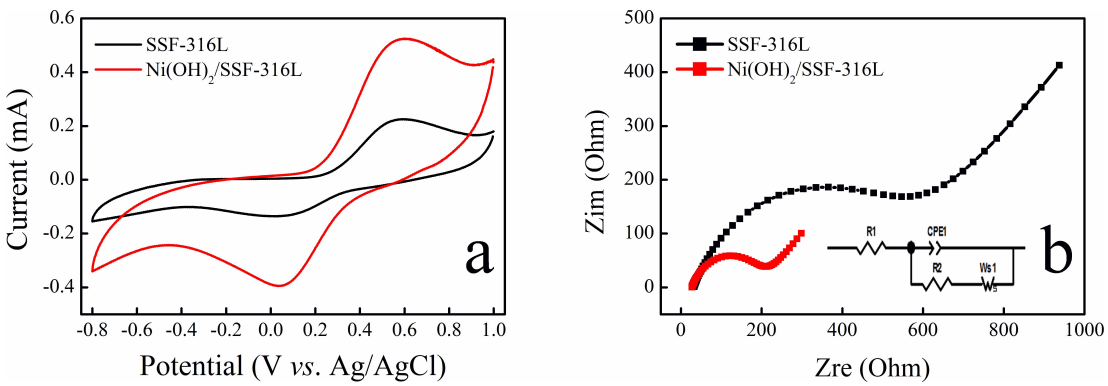

Fig. 3. (a) CV curves and (b) Nyquist plot of 1.0 mM $[Fe(CN)_6]^{3-/4-}$ in 0.1 M Na_2SO_4 at unmodified and $Ni(OH)_2$/SSF-316L [Inset: The equivalent circuit].

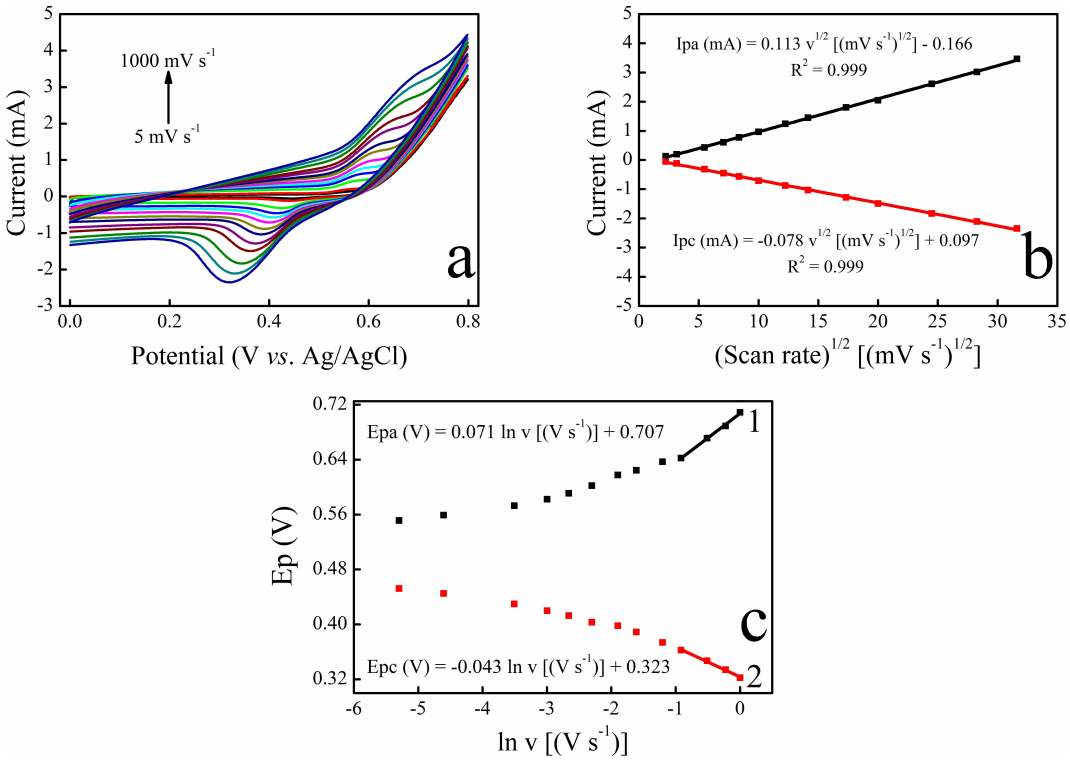

Fig. 4. (a) CV curves of $Ni(OH)_2$/SSF-316L in 0.1 M NaOH at scan rates of 5, 10, 30, 50, 70, 100, 150, 200, 300, 400,600, 800 and 1000 mV s^{-1}, (b) Dependence of the anodic and cathodic peak currents on the square root of the scan rate, (c) The dependency of anodic (1) and cathodic (2) peak potentials on ln v.

After the pretreatment detailed above, the electrocatalytic behavior of SSF-316L and $Ni(OH)_2$/SSF-316L was investigated using cyclic CV and EIS measurements in the absence and presence of glucose. Figure 5a shows the CV curves of the unmodified SSF-316L electrode in the absence and presence of glucose exhibited almost no oxidation peak and reduction peak, indicating that the unmodified SSF-316L had no response to glucose.

For the $Ni(OH)_2$/SSF-316L the anodic peak current increased significantly when 0.5 mM of glucose was added (Figure 5b).

In contrast, the cathodic peak current slightly decreased due to the consumption of Ni^{3+} in the electrooxidation of glucose. Meanwhile, the oxidation potential also shifted to more positive values, attributed to the faster glucose diffusion at the electrode surface. The oxidation mechanism of glucose to gluconolactone at the $Ni(OH)_2$/SSF-316L electrode surface is attributed, as reported in the literature, to the well-known catalytic effect of the Ni^{2+}/Ni^{3+} redox couple according to the following reactions:

$$Ni(OH)_2 + OH^- \Longleftrightarrow NiOOH + H_2O + e^- \quad (8)$$

$$NiOOH + glucose \Longleftrightarrow Ni(OH)_2 + glucolactone \quad (9)$$

Furthermore, EIS is used to investigate the electrochemical performance of the SSF-316L and $Ni(OH)_2$/SSF-316L electrodes in the absence and presence of glucose at 0.5 V of potential in a wide range of frequencies from 100 kHz to 0.1 Hz. The Nyquist diagram represents data about R_{ct} values, which are equal to semicircle diameters of the diagram.

Figure 5c indicates that the R_{ct} for the SSF-316L electrode in the absence of glucose is 635 Ohm. At the same time, this value decreases in the presence of glucose to reach 446 Ohm. However, the electron resistance of SSF-316L decreased remarkably after the electrochemical deposition of $Ni(OH)_2$ on the SSF-316L surface (Figure 5d). This semicircle becomes small without glucose (101 Ohm) and becomes much smaller after adding glucose (30 Ohm).

These results show that the charge transfer of $Ni(OH)_2$/SSF-316L is faster than that of the SSF-316L electrode. Therefore, CV and EIS diagrams support the successful preparation and excellent performance of $Ni(OH)_2$/SSF-316L.

The kinetics process during the electrooxidation of glucose was derived from the scan rates dependence obtained from CV grams. Figure 6a illustrates the CVs curves of $Ni(OH)_2$/SSF-316L electrode in 0.1 M NaOH solution with the addition of 0.5 mM of glucose over the range of scan rates 5–1000 mV s^{-1}. The anodic and cathodic peak currents (Ipa and Ipc) also increased when the scan rates increased.

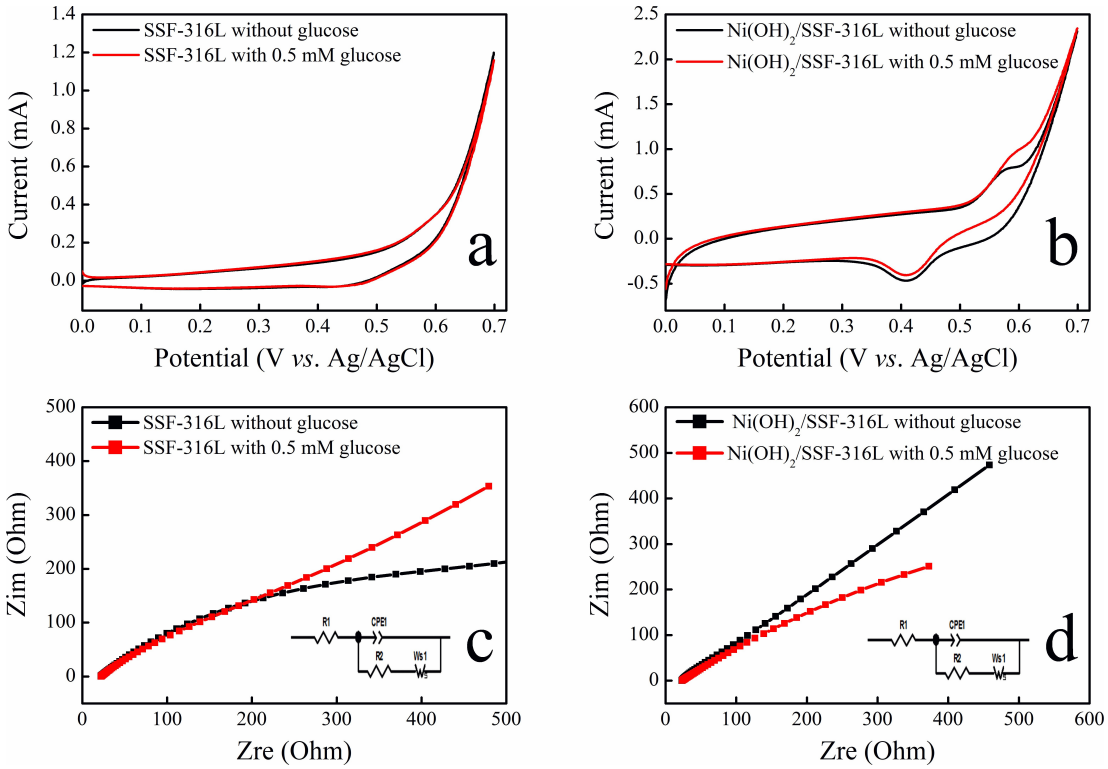

Fig. 5. CV curves of (a) unmodified and (b) $Ni(OH)_2$/SSF-316L before and after the addition of 0.5 mM glucose in an alkaline medium. Nyquist plots of (c) unmodified and (d) $Ni(OH)_2$/SSF-316L before and after addition of 0.5 mM glucose in 0.1 M NaOH solution. [The inset illustrates a corresponding equivalent circuit].

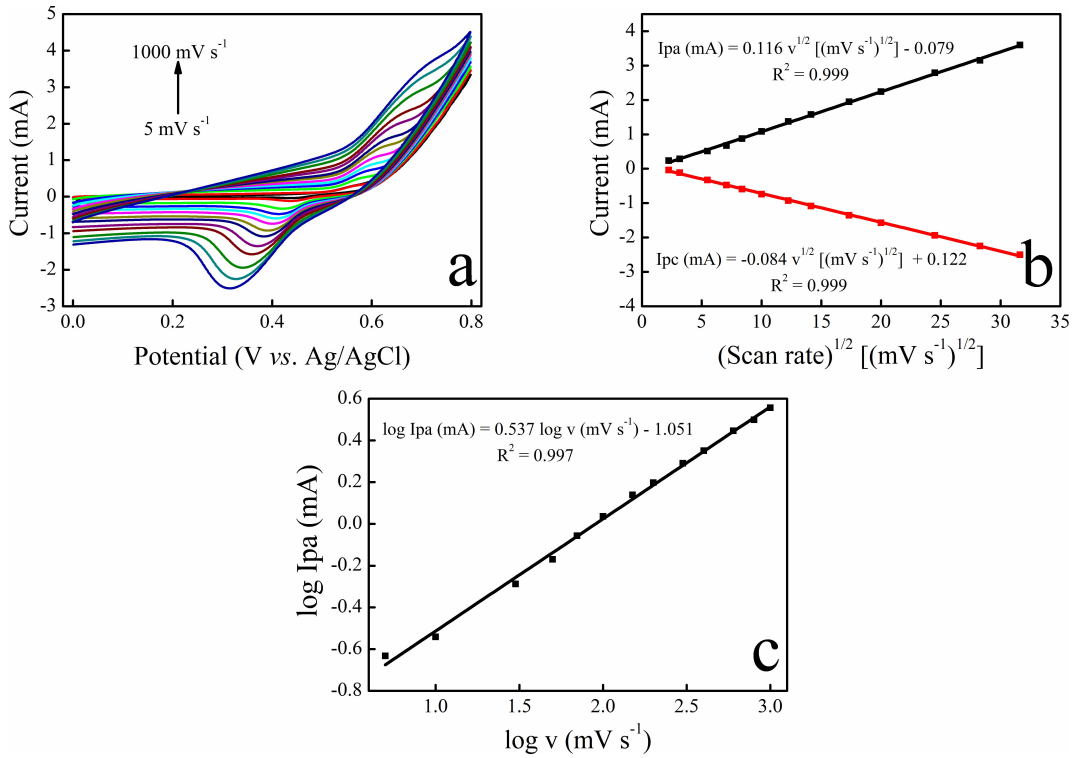

Fig. 6. (a) CV curves of 0.5 mM glucose in 0.1 M NaOH for different scan rates from 5 to 1000 $mV\,s^{-1}$ (b), Dependence of Ipa and Ipc *vs.* $v^{1/2}$, (c) Plot of log Ipa *vs.* log v.

Simultaneously, the anodic peak potential shifted positively, and the cathodic peak potential gradually shifted negatively. The relationship between Ipa and Ipc *vs.* $v^{1/2}$ revealed good linearity with a high correlation coefficient of 0.999 (Figure 6b). Thus, the modified electrode acting in a diffusion-controlled electrochemical process is advantageous for voltammetric and amperometric glucose detection. Furthermore, the plot of log Ipa vs. log v shows good linearity, with a slope very close to the theoretical value of 0.5 (Figure 6c), demonstrating the diffusion-controlled process for glucose oxidation on Ni-$(OH)_2$/SSF-316L electrode.

The chemical sensing ability of the fabricated electrode was characterized by both CV and amperometry techniques. Figure 7a shows the CVs behavior of the proposed electrode for consecutive additions of varying concentrations of glucose. It was revealed that anodic peak currents distinctly increase by increasing glucose concentration. Figure 7b presents two linear responses: the first from 5.0 µM to 1.0 mM and the second from 1.0 mM to 11 mM. Based on the first linear range, a limit of detection (LOD) was found corresponding to 10 µM.

Figure 7c shows the amperometric response of the $Ni(OH)_2$/SSF-316L electrode upon consecutive additions of glucose into a continuously stirred solution of 0.1 M NaOH under the applied potential of 0.55 V. The current-time curve shows an increase of oxidation peak current with glucose concentration. Figure 7d illustrates the calibration plot obtained from the amperometric curve. This latter shows two linear responses: the first one from 1.0 µM to 200 µM and the second from 200 µM to 4.0 mM.

In addition, the sensitivity was calculated from the first slope of the calibration curve, considering the linear region. The sensitivity was 1062 µA $mM^{-1}cm^{-2}$. The LOD of 2.0 µM (S/N = 3) was obtained, thus improving the obtained LOD using cyclic voltammetric measurements. Table 2 compares the analytic performance of $Ni(OH)_2$/SSF-316L with other foams-based glucose sensors. The results indicate that $Ni(OH)_2$/SSF-316L electrode is promising for glucose analytical application.

3.3 Anti-interference, Reproducibility, and Stability of the $Ni(OH)_2$/SSF-316L Sensor

The effects of some common interfering species such as L-ascorbic acid, acetaminophen, uric acid, and sucrose were studied using amperometry at the applied potential of 0.55 V. The $Ni(OH)_2$/SSF-316L electrode interference study was performed by adding 0.01 mM interferents and 0.2 mM glucose. These values are in a similar ratio level to those in normal physiological conditions [33]. No significant signals can be observed for interfering species (< 4 %) (Figure 8a). At the same time, two well-defined glucose oxidation current responses were obtained, implying the excellent selectivity for glucose oxidation by $Ni(OH)_2$/SSF-316L material-based sensor.

The reproducibility of five $Ni(OH)_2$/SSF-316L sensors separately prepared under the same conditions was

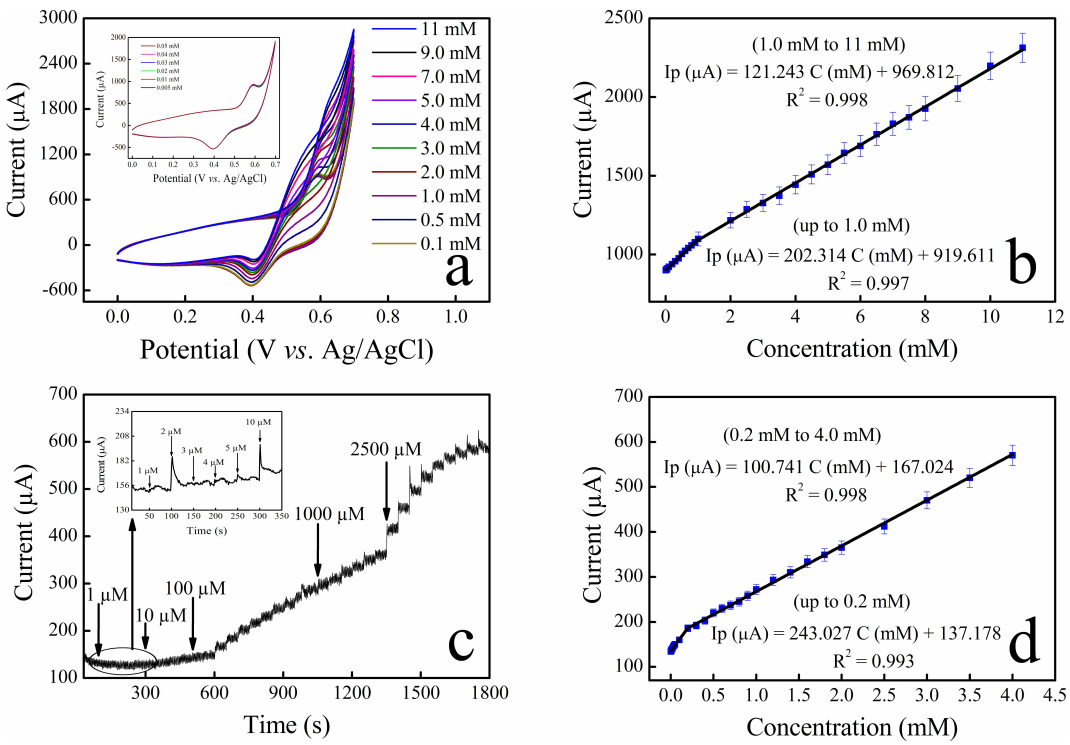

Fig. 7. (a) CV curves of $Ni(OH)_2$/SSF-316L with various glucose concentrations in 0.1 M NaOH solution at a fixed scan rate of 50 mV s^{-1}, (b) The corresponding calibration curves, (c) Amperometric response of $Ni(OH)_2$/SSF-316L electrode upon consecutive additions of glucose in 0.1 M NaOH solution at 0.55 V, (d) The corresponding calibration curves.

Table 2. Comparison of different foams-based nanomaterials for electrochemical detection of glucose.

Electrode	Limit of detection (μM)	Sensitivity ($\mu A\,mM^{-1}\,cm^{-2}$)	Linear range (mM)	Ref
$Ni(OH)_2$ nanowires/NiF	1.0	1598	0.1–6.0	[30]
Cu–Cu_2O NPs@3DGF	16.0	230.89	0.8–10	[45]
α-Fe_2O_3/NiF	0.87	10.35	0.005–0.2	[51]
PdNPs/Ni_5P_4-NF	0.91	242.5	0.002–4.65	[58]
BiOI/ZnO/NiF	2.0	115.2	0.01–3.25	[59]
NiO superstructures/NiF	6.15	395	0.018–1.2	[60]
Cu/NiF	2.0	–	0.006–0.206	[61]
α-$Ni(OH)_2$-rGO/NiF	–	95.5	0.5–22.5	[62]
$Ni(OH)_2$ nanosheets/NiF	1.0	1097	0.1–2.5	[63]
Ni foam	2.2	–	0.05–7.35	[64]
$Ni(OH)_2$/SSF-316L	2.0	1062	0.001–4.0	This work

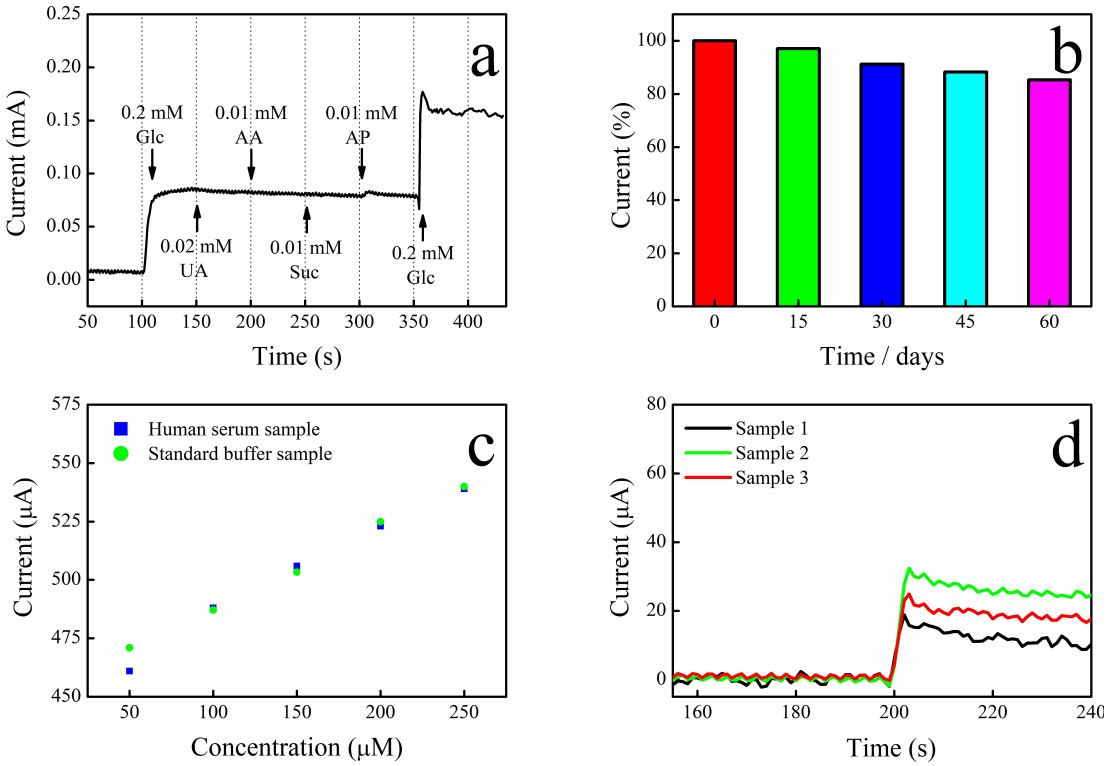

Fig. 8. (a) Chronoamperogram of $Ni(OH)_2$/SSF-316L with successive addition of Glc, UA, AA, AP, and Suc, (b) Illustration of current response of $Ni(OH)_2$/SSF-316L electrode towards 1.0 mM glucose in 0.1 M NaOH for two months, (c) Responses of the sensor to the same concentrations of glucose in human serum sample (blue) and in a standard sample (green), (d) Chronoamperogram of $Ni(OH)_2$/SSF-316L electrode with the addition of human serum to 0.1 M NaOH at an applied potential of 0.55 V.

investigated by measuring the current response of 1.0 mM glucose (Figure S2). The estimated relative standard deviation (RSD) was 2.48 %, indicating that the various sensors had good reproducibility. To assess repeatability, five successive amperometric measurements of 1.0 mM glucose with the same electrode were measured (Figure S3). The calculated RSD of the response current was 1.18 %, demonstrating excellent electrode repeatability. These findings suggest that the proposed $Ni(OH)_2$/SSF-316L sensor is not contaminated by glucose oxidation products and can be used repeatedly.

Furthermore, the long-term stability of the $Ni(OH)_2$/SSF-316L sensor was also estimated by measuring its amperometric response every fifteen days over two months (Figure 8b). The sensor was stored in a dry state between two measurements. The results showed only a reduction in the current response of 7 % for 1.0 mM glucose in an aqueous solution containing 0.1 M NaOH at a fixed potential of 0.55 V, indicating that the as-prepared $Ni(OH)_2$/SSF-316L electrode has good stability.

Table 3. Amperometric glucose sensor applied to human blood serum samples.

Samples	Concentration of glucose (mM) Proposed non-enzymatic method (mM)	Determined by a commercial glucometer (mM)	Recovery (%)
1	3.85	3.52	109.3
2	11.75	10.45	112.44
3	7.53	8.25	91.27

3.4 Determination of Glucose in Blood Serum Samples

The feasibility of $Ni(OH)_2$/SSF-316L was further examined using the same glucose concentrations in human blood serums and a standard sample. Figure 8c shows that the $Ni(OH)_2$/SSF-316L electrode had a close current response. Therefore, it can be used in real applications. The practical applicability of the $Ni(OH)_2$/SSF-316L sensor for real sample analysis was tested by a commercial glucometer and then by our sensor using amperometric measurements. I-t curves were recorded at 0.55 V (Figure 8d) in 10 mL of 0.1 M NaOH solution under stirring conditions with 10 µL blood serum injected. Table 3 summarizes the results obtained. The proposed sensor gave recoveries between 91.27–112.44 %, suggesting the potential application of $Ni(OH)_2$/SSF-316L for glucose determination in human blood serum.

4. Conclusion

For the first time, $Ni(OH)_2$ nanoparticles were successfully grown onto 316L stainless steel foam via a simple and facile electrochemical route using the CV method in an alkaline solution without nickel salts added. The analytical performance of the prepared electrodes was investigated by cyclic voltammetry and amperometric measurements.

Due to the unique nanostructure characteristics and active sites, the as-modified, $Ni(OH)_2$/SSF-316L foam electrode with optimum sensing potential 0.55 V characterized by a large surface area, and showed higher sensitivity 1062 µA $mM^{-1}cm^{-2}$, faster response time of 2 s and wider linear range of concentration (1.0 µM–4.0 mM), as well as low glucose detection value of 2.0 µM.

In addition, the proposed sensor can be used for glucose determination in real human blood serum with excellent selectivity accuracy. It revealed high stability and good reproducibility. Therefore, due to its good performance and low cost, the fabricated $Ni(OH)_2$/SSF-316L sensor could be used as a potential material for routine glucose analysis.

Acknowledgements

The authors would like to acknowledge the financial support from the General Direction of Scientific Research and Technology Development of the Algerian Ministry of Higher Education and Scientific Research.

Data Availability Statement

The data that support the findings of this study can be obtained from the corresponding author upon request.

References

[1] C. C. Cowie, K. F. Rust, E. S. Ford, M. S. Eberhardt, D. D. Byrd-Holt, C. Li, D. E. Williams, E. W. Gregg, K. E. Bainbridge, S. H. Saydah, L. S. Geiss, *Diabetes Care* **2009**, *32*, 287–294.
[2] S. A. Ross, E. A. Gulve, M. Wang, *Chem. Rev.* **2004**, *104*, 1255–1282.
[3] H. King, R. E. Aubert, W. H. Herman, *Diabetes Care* **1998**, *21*, 1414–1431.
[4] W. Raza, K. Ahmad, *Mater. Lett.* **2018**, *212*, 231–234.
[5] M. A. El-Shal, S. M. Azab, H. A. M. Hendawy, *Bull. Natl. Res. Cent.* **2019**, *43*, 95.
[6] Z. Xu, Q. Wang, H. Zhangsun, S. Zhao, Y. Zhao, L. Wang, *Food Chem.* **2021**, *349*, 129202.
[7] E. L. Rossini, M. I. Milani, H. R. Pezza, *Talanta* **2019**, *201*, 503–510.
[8] D. N. Lindqvist, H. Æ Pedersen, L. H. Rasmussen, *J. Chromatogr. B* **2018**, *1081*, 126–130.
[9] X. Chen, J. Chen, F. Wang, X. Xiang, M. Luo, X. Ji, Z. He, *Biosens. Bioelectron.* **2012**, *35*, 363–368.
[10] Y. C. Shen, A. G. Davies, E. H. Linfield, P. F. Taday, D. D. Arnone, T. S. Elsey, *J. Biol. Phys.* **2003**, *29*, 129–133.
[11] M. Hamtak, M. Hosseini, L. Fotouhi, M. Aghazadeh, *Anal. Methods* **2018**, *10*, 5723–5730.
[12] W. Q. Xie, Y. X. Gong, K. X. Yu, *J. Chromatogr. A.* **2017**, *1520*, 143–146.
[13] H. Xu, C. Xia, S. Wang, F. Han, M. K. Akbari, Z. Hai, S. Zhuiykov, *Sens. Actuators B* **2018**, *267*, 93–103.
[14] V. V. Khedekar, B. M. Bhanage, *J. Electrochem. Soc.* **2016**, *163*, 248–251.
[15] S. M. Babulal, S. M. Chen, R. Palani, K. Venkatesh, A. S. Haidyrah, S. K. Ramaraj, C. C. Yang, C. Karuppiah, *Colloids Surf. A* **2021**, *621*, 126600.
[16] S. Alexander, P. Baraneedharan, S. Balasubrahmanyan, S. Ramaprabhu, *Mater. Sci. Eng. C.* **2017**, *78*, 124–129.
[17] I. Osadebe, P. Conghaile, P. Kavanagh, D. Leech, *Electrochim. Acta* **2015**, *182*, 320–326.
[18] B. L. Zhang, Y. Yang, Z. Q. Zhao, X. D. Guo, *Electrochim. Acta* **2020**, *358*, 136917.
[19] J. C. M. Díaz-González, R. A. Escalona-Villalpando, L. G. Arriaga, S. D. Minteer, J. R. Casanova-Moreno, *Electrochim. Acta* **2020**, *337*, 135782.
[20] N. I. Chandrasekaran, M. Manickam, *Sens. Actuators B* **2019**, *288*, 188–194.
[21] Y. Li, M. Xie, X. Zhang, Q. Liu, D. Lin, C. Xu, F. Xie, X. Sun, *Sens. Actuators B* **2019**, *278*, 126–132.
[22] L. T. Hoa, N. T. Y. Linh, J. S. Chung, S. H. Hur, *Ionics* **2017**, *23*, 1525–1532.

[23] R. A. Soomro, O. P. Akyuz, R. Ozturk, Z. H. Ibupoto, *Sens. Actuators B* **2016**,*233*, 230–236.
[24] S. Nantaphol, T. Watanabe, N. Nomura, W. Siangproh, O. Chailapakul, Y. Einaga, *Biosens. Bioelectron.* **2017**, *98*, 76–82.
[25] X. Xu, H. Lv, L. Sun, P. Song, B. Liu, X. Chen, *ChemPlusChem* **2020**, *85*, 970–976.
[26] S. Khan, M. Iftikhar, M. A. Rasheed, M. Khan, S. Karim, A. Shah, M. Maqbool, G. Ali, *Appl. Nanosci.* **2019**, *9*, 2069.
[27] C. Karuppiah, M. Velmurugan, S. M. Chen, S. H. Tsai, B. S. Lou, *Sens. Actuators B* **2015**, *221*, 1299–1306.
[28] M. Velmurugan, N. Karikalan, S. Chen, *J. Colloid Interface Sci.* **2017**, *493*, 349–355.
[29] S. Guo, C. Zhang, M. Yang, Y. Zhou, C. Bi, Q. Lv, N. Ma, *Anal. Chim. Acta* **2020**, *1109*, 130–139.
[30] Q. Xiao, X. Wang, S. Huang, *Mater. Lett.* **2017**, *198*, 19–22.
[31] N. Karikalan, M. Velmurugan, S. M. Chen, C. Karuppiah, *ACS Appl. Mater. Interfaces* **2016**, *8*, 22545–22553.
[32] M. Baghayeri, A. Amiri, Z. Alizadeh, H. Veisi, E. Hasheminejad, *J. Electroanal. Chem.* **2018**, *810*, 69–77.
[33] C. W. Kung, Y. H. Cheng, K. C. Ho, *Sens. Actuators B* **2014**, *204*, 159–166.
[34] M. Adabi, M. Adabi, *J. Dispersion Sci. Technol.* **2021**, *42*, 262–269.
[35] H. Yin, J. Zhu, J. Chen, J. Gong, Q. Nie, *Mater. Lett.* **2018**, *221*, 267–270.
[36] M. L. Chelaghmia, M. Nacef, A. M. Affoune, M. Pontié, T. Derabla, *Electroanalysis* **2018**, *30*, 1117–1124.
[37] M. Nacef, M. L. Chelaghmia, A. M. Affoune, M. Pontié, *Electroanalysis* **2019**, *31*, 113–120.
[38] M. Usman, L. Pan, A. Farid, A. S. Khan, Z. Yongpeng, M. A. Khan, M. Hashim, *Carbon* **2020**, *157*, 761–766.
[39] M. L. Chelaghmia, M. Nacef, H. Fisli, A. M. Affoune, M. Pontié, A. Makhlouf, T. Derabla, O. Khelifi, F. Aissat, *RSC Adv.* **2020**, *10*, 36941–36948.
[40] M. Nacef, M. L. Chelaghmia, O. Khelifi, M. Pontié, M. Djelaibia, R. Guerfa, V. Bertagna, C. Vautrin-Ul, A. Fares, A. M. Affoune, *Int. J. Hydrogen Energy* **2020**, *46*, 37670–37678.
[41] I. Djaghout, A. M. Affoune, M. L. Chelaghmia, M. Bendjaballah, *Port. Electrochim. Acta* **2015**, *33*, 209–222.
[42] M. L. Chelaghmia, M. Nacef, A. M. Affoune, *J. Appl. Electrochem.* **2012**, *42*, 819–826.
[43] L. Jia, X. Wei, L. Lv, X. Zhang, X. Duan, Y. Xu, K. Liu, J. Wang, *Electrochim. Acta* **2018**, *280*, 315–322.
[44] S. Liu, W. Zeng, Y. Li, *Mater. Lett.* **2020**, *259*, 126820.
[45] Z. Khosroshahi, F. Karimzadeh, M. Kharaziha, A. Allafchian, *Mater. Sci. Eng. C* **2020**, *108*, 110216.
[46] X. Wang, H. Jian, Q. Xiao, S. Huang, *Appl. Surf. Sci.* **2018**, *459*, 40–47.
[47] Y. Zhang, D. Zhao, W. Zhu, W. Zhang, Z. Yue, J. Wang, R. Wang, D. Zhang, J. Wang, G. Zhang, *Sens. Actuators B* **2018**, *255*, 416–423.
[48] W. Mao, H. He, Z. Ye, J. Huang, *J. Electroanal. Chem.* **2019**, *832*, 275–283.
[49] Y. Lu, B. Jiang, L. Fang, S. Fan, F. Wu, B. Hu, F. Meng, *Electroanalysis* **2017**, *29*, 1–8.
[50] W. Liu, X. Wu, X. Li, *RSC Adv.* **2017**, *7*, 36744–36749.
[51] Y. Liu, W. Zhao, X. Li, J. Liu, Y. Han, J. Wu, X. Zhang, Y. Xu, *Appl. Surf. Sci.* **2020**, *512*, 145710.
[52] R. Prathipati, R. Ch, S. P. Dora, *SN Appl. Sci.* **2019**, *1*, 1–11.
[53] A. V. Ingle, V. S. Raja, J. Rangarajan, P. Mishra, *Int. J. Hydrogen Energy* **2020**, *45*, 3094–3107.
[54] A. G. M. Ferrari, C. W. Foster, P. J. Kelly, D. A. C. Brownson, C. E. Banks, *Biosensors* **2018**, *8*, 53–63.
[55] M. L. Chelaghmia, H. Fisli, M. Nacef, D. A. C. Brownson, A. M. Affoune, H. Satha, C. E. Banks, *Anal. Methods* **2021**, *13*, 2812–2822.
[56] M. Mathew, N. Sandhyarani, *Electrochim. Acta* **2013**, *108*, 274–280.
[57] E. Laviron, *J. Electroanal. Chem.* **1979**, *101*, 19–28.
[58] M. Wang, Z. Ma, J. Li, Z. Zhang, B. Tang, X. Wang, *J. Colloid Interface Sci.* **2017**, *511*, 355–364.
[59] M. Zhao, J. Shang, H. Qu, R. Gao, H. Li, S. Chen, *Anal. Chim. Acta* **2020**, *1095*, 93–98.
[60] L. Wang, Y. Xie, C. Wei, X. Lu, X. Li, Y. Song, *Electrochim. Acta* **2015**, *174*, 846–852.
[61] G. Melinte, A. Cernat, A. Petica, O. Lazar, M. Enachescu, L. Anicai, C. Cristea, *Materials* **2020**, *13*, 1–16.
[62] M. Dong, H. Hu, S. Ding, C. Wang, *J. Mater. Sci. Mater. Electron.* **2021**, *32*, 19327–19338.
[63] Y. Zhao, G. Gu, S. You, R. Ji, H. Suo, C. Zhao, F. Liu, *RSC Adv.* **2015**, *5*, 53665–53670.
[64] W. Lu, X. Qin, A. M. Asiri, A. O. Al-Youbi, X. Sun, *Analyst* **2012**, *138*, 417.

Received: December 27, 2021
Accepted: April 11, 2022
Published online on ■■, ■■

RESEARCH ARTICLE

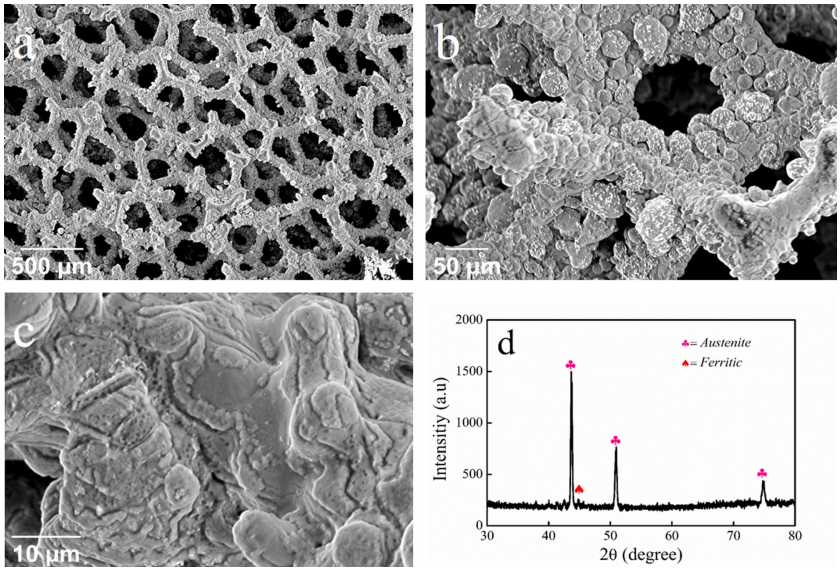

W. Drissi, M. Lyamine Chelaghmia, M. Nacef, A. Mohamed Affoune, H. Satha, R. Kihal, H. Fisli, C. Boukharouba, M. Pontié*